Optimizing mechanical properties and print accuracy of 3D printed lightweighting continuous fiber reinforced PLA foams

Kui Wang[1], Xinru Li[1], Ping Cheng[1,2,*], Donghua Zhao[3], Yi Xiong[3], Wei Wen[4], Yong Peng[1], Said Ahzi[2]

1. Key Laboratory of Traffic Safety on Track of Ministry of Education, School of Traffic and Transportation Engineering, Central South University, Changsha 410075 China;
2. ICUBE Laboratory-CNRS, University of Strasbourg, Strasbourg 67000, France;
3. School of System Design and Intelligent Manufacturing, Southern University of Science and Technology, Shenzhen, 518055, China;
4. School of Engineering, Lancaster University, Lancaster LA1 4YW, UK
[*]Corresponding author: ping.cheng@etu.unistra.fr

Author Contributions

Kui Wang: Conceptualization, Methodology, Writing—review and editing, Supervision. **Xinru Li:** Conceptualization, Methodology, Data curation, Writing—original draft. **Ping Ching:** Methodology, Writing—review and editing, Supervision. **Donghua Zhao:** Methodology, writing—review and editing. **Yi Xiong:** Validation. **Wei Wen:** Supervision. **Yong Peng:** Validation. **Said Ahzi:** Validation.

Acknowledgements

The authors would like to acknowledge the financial support of the Natural Science Foundation of Hunan (2024JJ5434) and the Postdoctoral Fellowship Program of CPSF (GZC20240646)

Abstract: Due to the urgent demand for lightweight and high-strength materials in rail transportation, this study proposed foamed polylactic acid (PLA) composites reinforced with continuous basalt fibers (BF) using 3D printing technique to address the limitations posed by foaming-induced strength reduction in foam. Through a combination of parametric calculations, microscopic observations, and compression experiments, the effects of printing parameters on the expansion ratio and print accuracy of foamed composite were investigated. It was found that adding fibers to foamed PLA reduced the expansion ratio of PLA by up to 9.52% at lower printing temperatures and layer heights but increased it at higher settings. The expansion ratio of the composite significantly increased with high printing temperatures and layer heights. When the composites were fabricated at low print temperatures and high layer heights, noticeable interlayer gaps and exposed fibers leading to poor impregnation were observed at cross section. This phenomenon was improved as the expansion ratio increased. In addition, specimens with optimal print accuracy were prepared at specific combinations of printing temperature and layer height. In light of this discovery, a predictive function based on combined printing parameters was established to design composites with excellent print accuracy and specific densities. Finally, compression test results showed that with the same density of 0.5 g/cm^3, the foamed composite exhibited substantial improvements in compressive strength, modulus, and strain energy density compared to the foamed PLA, with increases of 44.44%, 57.02%, and 24.19%, respectively.

Keywords: lightweighting; foaming; continuous fiber; composites; 3D printing

Highlights

- The foamed PLA composites reinforced with continuous basalt fibers using 3D printing technique was first proposed.
- The effects of printing parameters on the expansion ratio and print accuracy of foamed composites were investigated.
- The predictive function of printing parameters was established to manufacture composites with excellent print accuracy and specific densities.

1. Introduction

Polymeric foams, composed of solid polymer and gaseous phases [1,2], are widely used in construction, packaging, automotive sectors, insulation appliances, and transportation owing to their high strength-to-weight ratio, excellent heat insulation and energy absorption ability [3−5]. In the railway transportation, polymeric foams are integral to enhancing vehicle performance, safety, and passenger comfort. The exceptional energy absorption properties of these foams make them crucial for mitigating impacts and vibrations, thereby improving safety and comfort. In rail transportation, polymeric foams are utilized in train carriages, vehicle interiors, and insulation materials, where they effectively absorb impact energy, reduce noise, and dampen vibrations. Additionally, their lightweight nature contributes to the reduction of overall train weight, enhancing fuel efficiency and reducing emissions. Polymeric foams can be produced using a variety of polymers, such as polyurethane (PU), polystyrene (PS), polyvinyl chloride (PVC), polyethylene (PE), or polypropylene (PP) [6,7]. However, the large-scale production and utilization of non-biodegradable foams pose significant environmental threats, highlighting the importance of biodegradable polymer foam materials [8]. Polylactic acid (PLA) foams, known for their superior biocompatibility, excellent processing performance, and high permeability, are a common biodegradable polymer material with numerous industrial applications [9,10].

In the literature, injection modeling, supercritical foaming molding, and bead foaming, have been extensively applied as the most common traditional manufacturing methods in the production and research of polymeric foams [11−13]. Nowadays, a technique integrates hollow microspheres into the initial materials of additive manufacturing, such as thermoplastic filaments, enabling the 3D printing of foams and integrating the strengths of additive manufacturing (AM) and foam structures [14−17]. The investigation of printing principles and the effect of various parameters on the density, expansion ratio, and mechanical characteristics of foamable polymers produced through 3D printing has garnered significant interest from researchers. Tammaro et al [16] developed a cost-effective 3D printing technique that produced materials with complex foamed morphologies and explored the effect of printing parameters on foaming efficiency. They found that the size and density of the bubble, as well as crystallinity, highly depended on the CO_2 concentration and processing temperature. Pawar et al. [18] achieved control of foam material properties by adjusting the 3D printing parameters. They investigated the effects of temperatures, layer height, and nozzle diameter on the density of the polymeric foams. The results demonstrated that the density and expansion ratio of the foamed material were notably affected by the 3D printing parameters.

Nevertheless, the relatively poor strength of foamed PLA limited its application range, making methods

to enhance the materials' strength a focal point in research [19,20]. In recent years, common approaches to increasing the strength of foamed polymers included altering the chemical composition and structure of the polymer, modifying process conditions, and incorporating specified additives [21,22]. Among these methods, the incorporation of additives such as graphene, fibrin, short fibers emerged as a straightforward approach to enhancing polymer strength. Wang et al. [23] conducted a study on the fabrication of a robust chopped glass fiber (GF)-reinforced PLA foamed composite (PLA/GF) using supercritical carbon dioxide foaming. They investigated the foaming behavior and mechanical properties of PLA/GF composites. The results indicated that PLA/GF composites exhibited higher compressive strength and modulus when compared to pure PLA foams. However, the improvement of mechanical properties of foams by short fibers was relatively limited. Consequently, continuous fiber were expected to further improve foam materials' mechanical properties [24,25]. Particularly, basalt fibers (BF), known for their high strength, lightweight, and resistance to extreme temperatures and corrosion, are considered high-performance materials. Based on these properties, basalt fiber composites have a wide range of applications, including in the structural and interior components of rail transit vehicles.

In this study, foamed composites reinforced with continuous basalt fibers (PLA/BF) were fabricated via the 3D printing technique. The different expansion ratio between foamed composite and foamed PLA and the effects of printing parameters on the expansion ratio, interlayer gaps, and print accuracy of foamed composite were systematically investigated. Additionally, a predictive method for determining printing parameters corresponding to various composite densities was developed by optimizing the print accuracy. The compression responses and energy absorption characteristics of the specific density PLA/BF composites were compared with those of foamed PLA through quasi-static compression tests.

2. Materials and methods

2.1. Materials

Lightweight polylactic acid filament (PLA-LW) from eSUN (Shenzhen, China) and continuous basalt fiber from Haining Anjie Composite Material Co., Ltd. (Zhejiang, China) were used in this study. PLA-LW filament had a diameter of 1.75 mm, a density of 1.21 g/cm^3, and thermally expandable microspheres (TEMs), which were the critical components of the foamed filament. Heating TEMs led to an increase in microsphere size, causing foaming. The recommended extruder temperature range for PLA-LW was 190 °C to 270 °C to achieve different expansion ratios. The density and linear density of the continuous basalt fiber were 2.64 g/cm³ and 62 tex, respectively.

2.2. Specimen preparation

Composite specimens were fabricated using modified in-situ impregnation 3D printing equipment with a 1.35 mm nozzle diameter. Figure 1 illustrates the schematic presentation of the fabrication process for continuous fiber-reinforced foamed composite specimens by 3D printing process.

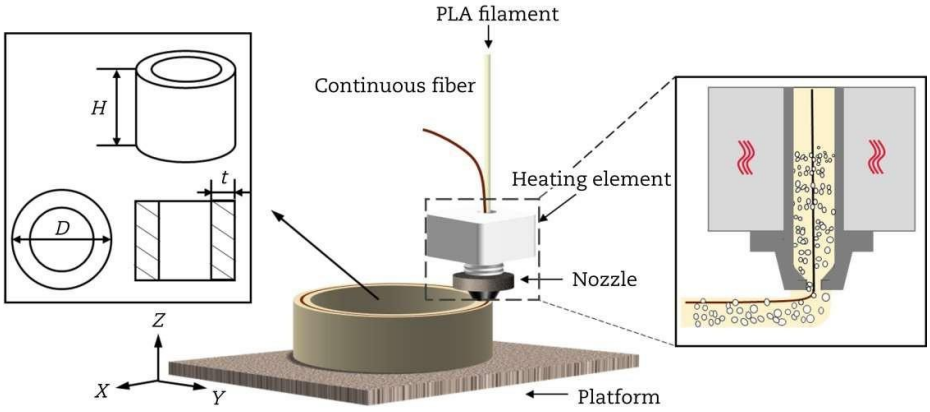

Fig. 1. Schematic diagram of continuous fiber-reinforced foamed composite fabricated by 3D printing process

The polymer filament and basalt fiber were introduced into the nozzle, heated to the specified temperature, and deposited on the printer platform along a planned path, accompanied by high-speed foaming. In this process, the layer height between the nozzle and the print bed limited the expansion of the foaming in the Z-direction. Therefore, a cylindrical ring specimen was selected to allow free volume expansion, with a diameter of 40 mm and ten layers. Additionally, cylindrical structures are widely used in rail transportation for energy absorption and lightweight support. The print trajectory was designed using Gcode from the slicing software ideaMaker.

According to previous studies, the variations in printing temperature and layer height had a more significant influence on the expansion ratio and density of the 3D printed foams, affecting sample dimensional accuracy and mechanical properties than other processing parameters [4,18,26−28]. Thus, these two printing parameters were chosen as variables in this study.

The printing temperature T_n used in this research increased by 20 °C, from 190 °C to 270 °C. The layer height h was set to a minimum of 0.3 mm to avoid the breakage of continuous fiber due to the limited space between the nozzle end, and a maximum of 0.6 mm to prevent delamination between layers, with an increment of 0.1 mm. As shown in Table 1, the other printing parameters, such as printing speed (v) and bed temperature (T_b) had no significant effect on the foaming process and were therefore kept constant. Figure 2 shows the composite specimens printed under the set parameters.

Table 1. Used 3D printing parameters

Parameter	Value
Printing temperature, T_n/°C	190, 210, 230, 250, 270
Bed temperature, T_b/°C	50
Printing speed, v/(mm·min^{-1})	200
Extrusion rate, E/(mm·min^{-1})	0.25
Nozzle diameter, ND/mm	1.35
Layer height, h/mm	0.3, 0.4, 0.5, 0.6

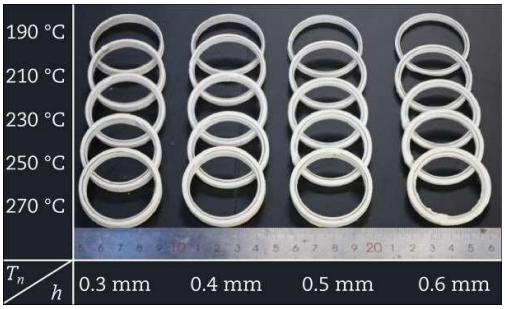

Fig. 2. Specimens fabricated with different printing parameters

2.3. Characterizations

Five repetitive tests for each specimen were carried out in the experiment, and the average values were calculated along with their standard deviations. The density of the specimen was calculated using the following equation:

$$\rho = \frac{m}{\pi\left\{\frac{\bar{D}^2}{4}-\left(\frac{\bar{D}}{2}-\bar{t}\right)^2\right\}\times\bar{H}} \tag{1}$$

where m was the measured weight of the specimens in the air, $\overline{D}$, $\overline{H}$ and $\bar{t}$ were the average values of the outer diameter, thickness, and height of the rings measured by vernier calipers, respectively. The expansion ratio Φ was given by Eq. (2) [29]:

$$\Phi = \left(1-\frac{\rho_f}{\rho_b}\right)\times 100\% \tag{2}$$

where ρ_b was the density of the unfoamed PLA, 1.21 g/cm^3, and ρ_f was the density of the foamed PLA, which could be calculated as:

$$\rho = \frac{m-m_{BF}}{\pi\left\{\frac{\bar{D}^2}{4}-\left(\frac{\bar{D}}{2}-\bar{t}\right)^2\right\}\times H-\frac{m_{BF}}{\rho_{BF}}} \tag{3}$$

where m_{BF} was the fiber weight used in the specimen. In this study, the relative accuracy δ_R along the height (H) direction reflected the changes in specimen height and characterized dimensional accuracy. It was calculated as follows [30]:

$$\Phi = \left(\frac{H-H_t}{H_t}\right)\times 100\% \tag{4}$$

where H_t denoted the designed height of the expanded specimens.

In this study, the temperature field measurement system (Mengchen MCDC-310, Hunan Ruoxin Co., Ltd, China), consisting of a thermal imaging camera, was utilized to monitor the temperature during printing.

The mechanical properties of the composite were determined through quasi-static radial compression tests. Quasi-static radial compression tests were performed to investigate how fibers reinforce the foamed matrix, a key factor governing the composites' mechanical performance under compression. These tests were conducted at room temperature using a universal material testing machine (E44, MTS Systems Co., Eden Prairie, MN, USA). During compression, specimens were placed on a rigid bottom plate, and the upper plate applied a constant loading velocity of 5 mm/min [31]. The experimental data were processed to derive the

compressive stress (σ)-strain (ε) response curve and strain energy density (W) by the following equations [32].

$$\sigma = F/A \tag{5}$$

$$\varepsilon = x/D \tag{6}$$

$$W = \int \sigma d\varepsilon \tag{7}$$

where F was the compression load, A was the initial ring projection area, $A=H\times D$, and x was the compression displacement.

3. Results and discussion

3.1. Material density and expansion ratio

To study the effects of nozzle temperature and layer height on material density and foaming, the effect of fibers was first analyzed. This study compared the expansion ratios of PLA and PLA/BF specimens under six representative printing parameters. As shown in Fig. 3, the addition of fibers slightly reduced the expansion ratio of PLA at lower temperatures and layer heights. For instance, at a layer height of 0.3 mm and a nozzle temperature of 230 °C, the expansion ratio of PLA/BF was 9.52% lower than that of PLA. However, with the temperature and layer height increased, PLA/BF exhibited a greater expansion ratio compared to PLA. Overall, the composite maintained the lightweight characteristics of foamed PLA and provided a suitable basis for investigating the influence of printing parameters on material expansion ratio.

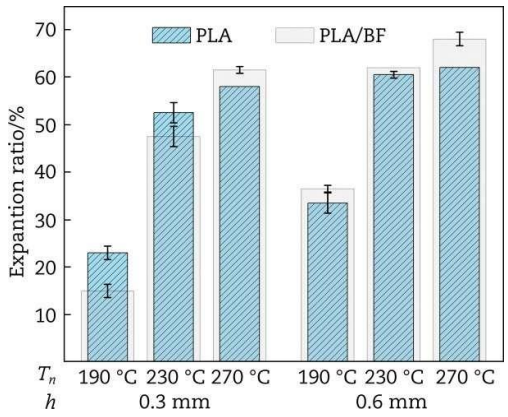

Fig. 3. Expansion ratios of PLA/BF and PLA specimens with different printing parameters

The influence of printing parameters on the density and expansion ratio of specimens is depicted in Fig. 4. As the printing temperature or the layer height increased, specimen density decreased (Fig. 4(a)). The lowest density of 0.41 g/cm³ was achieved at a nozzle temperature of 270 °C and a layer height of 0.6 mm.

Increasing the printing temperature from 190 °C to 270 °C while maintaining a constant layer height reduced the density by 53.27%. Similarly, increasing layer height from 0.3 mm to 0.6 mm progressively decreased the specimen density at a given printing temperature, with the reduction being more significant at lower temperatures.

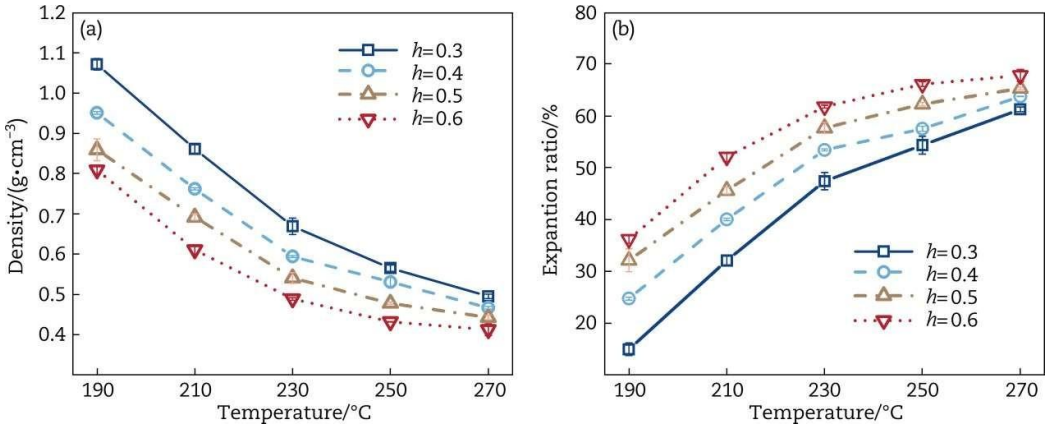

Fig. 4. Effects of printing temperature and layer height on (a) the density, and (b) the expansion ratios of PLA/BF

Figure 4(b) illustrates the influence of printing temperature and layer height on the expansion ratio of the specimen. The results showed a minimum expansion ratio of 15.00% at a layer height of 0.3 mm and a nozzle temperature of 190 °C, and a maximum expansion ratio of 67.78% at a layer height of 0.6 mm and a nozzle temperature of 270 °C. Increasing the nozzle temperature from 190 °C to 270 °C at a layer height of 0.3 mm resulted in a 308.27% increase in the expansion ratio. Similarly, changing the layer height from 0.3 mm to 0.6 mm at a nozzle temperature of 190 °C led to a maximum expansion ratio increase of 141.33%.

As shown in Fig. 5, a microstructure of the printed foamed composites at different printing parameters was analyzed to explain the relationship between the print parameters and the expansion rate (Fig. 4). As indicated by the yellow dashed line in Fig. 5(a), the inter-layer gaps and deposited layer boundaries were distinguishable at a nozzle temperature of 190 °C and a layer height of 0.5 mm. However, as the nozzle temperature increased to 270 °C, these features became increasingly difficult to discern, as shown in Fig. 5(b). Notably, these gaps could significantly influence the mechanical properties of the printed composites [33].

Furthermore, as indicated by the blue arrows in Figs. 5(a1), some of the TEMs remained unexpanded. Increasing the nozzle temperature from 190 °C to 270 °C resulted in a marked increase in the number and diameter of the foams, along with a reduction in their thickness, as shown in Figs. 5(b1). This study revealed that the printing temperature significantly influenced the density and expansion ratio of the material by controlling the degree of TEM expansion, as evidenced by the observable changes in the internal microstructure. At a fixed printing temperature of 230 °C, the sample at with a layer height of 0.6 mm exhibited more pronounced interlayer gaps compared to the specimen with a layer height of 0.3 mm (Figs. 5(c, d)). However, increasing the layer height from 0.3 mm to 0.6 mm did not affect the number and diameter of the foams, as shown in Figs. 5(c1, d1). Based on these microscopic observations, the reduction in density increased interlayer gaps resulting from higher layer heights, and enhanced foam content and diameter due to increased printing temperatures.

The interfacial interactions between the continuous BF and foamed PLA matrix were investigated in Figs. 5(a2, b2). As shown in Fig. 5(a2), at a layer height of 0.5 mm and a nozzle temperature of 190 °C, the fibers were primarily distributed within the gaps between layers, with minimal matrix adhering to the BF. This indicated poor impregnation of the fibers by the matrix, leading to weak interfacial adhesion between the BF and the PLA matrix. In contrast, Fig. 5(b2) presented a different phenomenon, which the BF bundles were tightly enveloped by matrix, with virtually no gaps at a layer height of 0.5 mm and a nozzle

temperature of 270 °C. The matrix fully penetrated the fiber bundles, confirming more effective impregnation compared to Fig. 5(a2). This observation suggested an optimal combination of the printing temperature and layer height could reduce interlaminar gaps and improve interfacial adhesion and impregnation, thereby enhancing the properties of the composite [34].

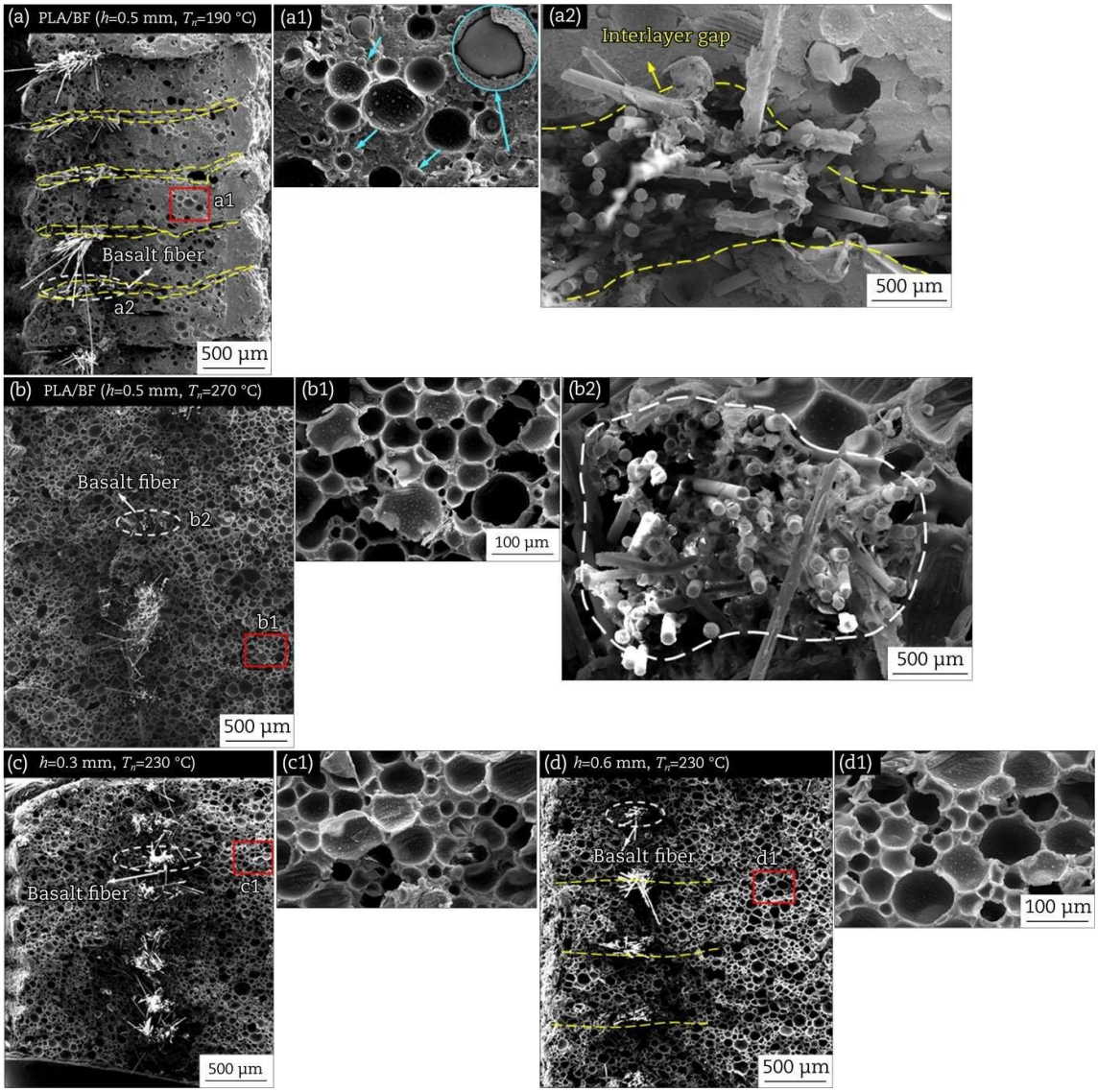

Fig. 5. Effects of printing parameters temperature (a−b), layer height (c−d) on the cross-sectional microstructure of foamed composites

3.2. Ring thickness and geometrical accuracy

The foamed composite ring fabricated by fused filament fabrication (FFF) exhibited complex expansion behavior along its thickness (t) within a specific range influenced by printing parameters. As shown in Fig. 6(a), the ring thickness significantly increased with rising nozzle temperature. At a layer height of 0.3 mm, a maximum thickness of 4.3 mm was attained at a nozzle temperature of 270 °C, representing a 68.93% increase compared to that at 190 °C. This increase was attributed to the expansion ratio rising at higher temperatures, resulting in volume expansion towards the ring thickness [19]. Conversely, increasing the layer height from 0.3 mm to 0.6 mm resulted in a maximum decrease in ring thickness of 25.05% at a nozzle temperature of 190 °C.

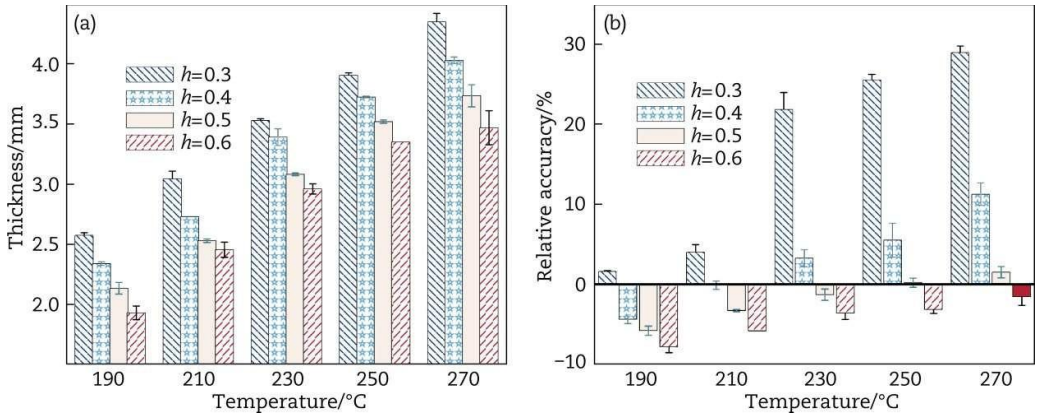

Fig. 6. Effects of printing temperature and layer height on (a) the ring thickness, and (b) the relative accuracy of height

As shown in Fig. 6(b), the relative accuracy along the vertical direction (as defined in Eq. (3)) varied significantly with changes in printing temperature and layer height. For instance, at a layer height of 0.4 mm and a nozzle temperature of 190 °C, the relative accuracy, δ_R, was −4.38%, indicating that the printed specimen was undersized compared to the intended design specifications. In contrast, at a nozzle temperature of 210 °C, δ_R was 0.00%, representing optimal printing accuracy. As the temperature further increased, the deviation of the specimen became more significant and tended to be positive values, indicating oversizing of the height compared to the designed specimen. The effect of layer height on relative accuracy followed a similar pattern. The relative accuracy varied with layer height, showing positive, zero, and negative values. At a nozzle temperature of 250 °C, the relative accuracy was 25.50% at a layer height of 0.3 mm, 0% at 0.5 mm, and −3.15% at 0.6 mm. Negative values of relative accuracy indicated low foaming and insufficient volume expansion of the material. As shown in Fig. 6, the relative accuracy of 28.92% was considered relatively positive when the nozzle temperature was 270 °C and the layer height was 0.3 mm.

Figure 7 illustrates the distribution of temperature and layer height during the printing. During the printing of the last layer, the temperature of the initial layer exceeded the minimum foaming temperature by 190 °C. The temperature of the final layer just below the nozzle reached 240 °C, then decreased to 190 °C after approximately 5 seconds, as determined based on the printing speed. Consequently, after the nozzle was removed, the pressure exerted by the nozzle ceased, causing most of the material to expand vertically.

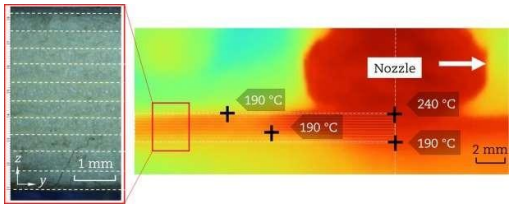

Fig. 7. Temperature distribution during printing and layer height distribution of the specimen at h=0.3 mm and T_n=270 °C

3.3. Printing parameters prediction

In the traditional FFF method, slicing software directly set the parameters without considering the crucial correlation between volume expansion and variable parameters. Therefore, calculating appropriate printing parameters for the efficient production of foamed specimens was essential. As shown in Fig. 3(a) and Fig. 5(c), negative relative accuracy ($\delta_R < 0$) resulted in poor interlayer bonding due to insufficient foaming and volume expansion. This led to visible interlayer gaps and lower density, as evidenced by the density of 0.49 g/cm³ at $\delta_R = -3.58\%$. On the other hand, positive relative accuracy ($\delta_R > 0$) was associated with excessive foaming and volume expansion. While this eliminated interlayer gaps, it also significantly

increased density, as demonstrated by the density of 0.67 g/cm³ at δ_R = 21.83%. These results revealed a trade-off between density and interlayer bonding: higher density improved interlayer adhesion at the expense of foaming efficiency, whereas lower density enhanced foaming but weakened interlayer bonding. Therefore, achieving a relative accuracy close to zero ($\delta_R \approx 0$) is essential to balance these competing factors. At $\delta_R = 0$, the material exhibited optimal interlayer bonding with minimal gaps and relatively high density, representing the best compromise between foaming efficiency and structural integrity. This study demonstrates that $\delta_R = 0$ is the optimal target for simultaneously maximizing interlayer adhesion and controlling density in foamed composite fabrication. This study defined this layer height (h) as the optimal height h^* for that temperature. Additional information about h^* was gathered, and the relative accuracy data was fitted using the following exponential decay function (expDec1):

$$y = y_0 + Ae^{-x/t} \tag{8}$$

As shown in Fig. 8, this process identified the optimal height (h^*) values for achieving zero relative accuracy at various nozzle temperatures. The h^* values were determined to be 0.32 mm at 190 °C, 0.40 mm at 210 °C, 0.47 mm at 230 °C, 0.50 mm at 250 °C, and 0.55 mm at 270 °C. These five sets of optimal parameters were used to prepare the specimens mentioned below, and the corresponding results were summarized in Table 2. The data confirmed that the relative accuracies of all five specimen sets remained within the range of ±1.25%.

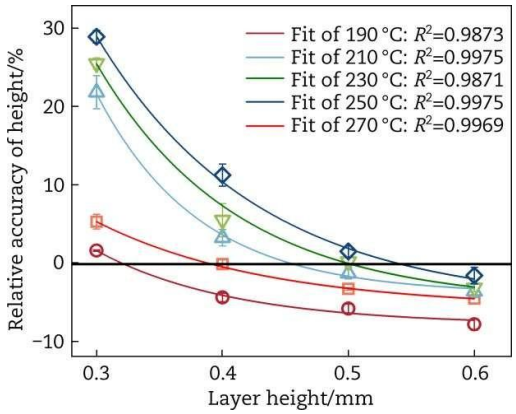

Fig. 8. Fitting curves of the relationship between layer height h and relative height accuracy δ_R

Table. 2. Relative accuracies and densities of the specimens with different optimized parameters

Temperature/°C	H_t/mm	H/mm	δ_R/%	ρ/(g·cm^{-3})
190	3.2	3.24	1.25	1.05
210	4	3.99	−0.25	0.76
230	4.7	4.75	1.06	0.56
250	5	4.98	−0.40	0.48
270	5.5	5.5	0	0.42

To extend the application of the parameter prediction method, determining optimal layer heights for various temperatures was essential. Figure 9(a) presents the results of a regression analysis using data from Table 2 to establish an equation relating printing temperature (T_n) to the optimal layer height (h^*).

$$h* = -0.1825 + 0.00275 \times T_n \quad (9)$$

Given that h^* varied with nozzle temperature, the density also varied nonlinearly within our study range of temperatures. Therefore, a sigmoidal curve was employed for fitting via ordinary least squares (OLS), which exhibited superior convergence compared to other methods, as described in Eq. (10):

$$p = 142.83 \times exp(T_n/35.82) + 0.34 \quad (10)$$

As depicted in Fig. 9(b), the exponential function fitted well, and the regression model demonstrated a high degree of goodness of fit, accurately predicting the outcome variable. These results indicated that the model effectively explained a significant portion of the data's variation, with minimal residuals—desirable attributes in regression analysis. This robust fit suggested that the model was suitable for further research and predictive applications.

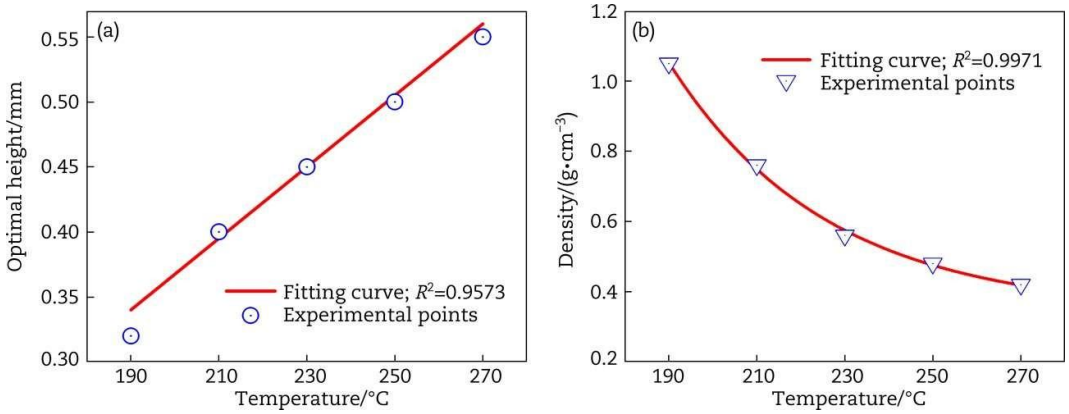

Fig. 9. Fitting curves according to the function on temperature and optimal height (a), temperature and density (b)

To validate the proposed prediction method, specimens were prepared at predetermined densities of 0.9 g/cm^3 and 0.5 g/cm^3 using printing temperatures and layer heights calculated via Eqs. (7) and (8). The predicted corresponding layer heights were 0.36 mm and 0.48 mm, whereas the temperatures were 198 °C and 243 °C. The predicted layer heights were 0.36 mm and 0.48 mm, respectively, at temperatures of 198 °C and 243 °C. The deviations from the target densities were 1.33% and -4.00%, with corresponding relative accuracies of −3.78% and 2.67%. These results confirmed the accuracy and effectiveness of the prediction approach.

3.4. Mechanical characterization

The above validation specimens were further considered for their mechanical properties and fiber reinforcement effect. Figure 10 shows the crushing processes and the collapse response strain-stress curves of the compression specimens with densities of 0.9 g/cm³ and 0.5 g/cm³. During the initial elastic stage, the stress increased rapidly. Subsequently, pairs of plastic hinges formed at the horizontal and vertical central positions, causing the strain-stress curves to reach a plateau stage. In the lower density specimen (0.5 g/cm³), the first cracks appeared along the plastic hinge lines.

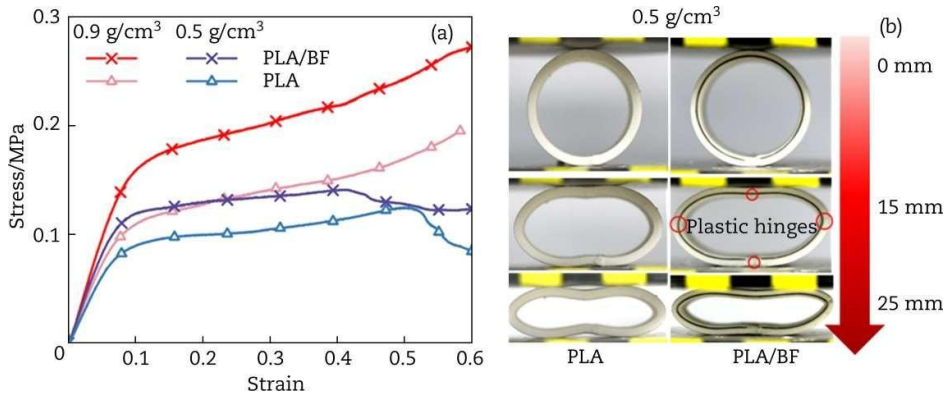

Fig. 10. Stress-strain curves (a) and deformation processes of foamed PLA and PLA/BF specimens (b)

The mechanical properties of foamed PLA and foamed PLA/BF at different densities as shown in Fig. 11. The compression test results indicated that as the density decreased from 0.9 g/cm³ to 0.5 g/cm³, the compressive strength, modulus, and strain energy density of the foamed PLA material decreased by 18.18%, 13.57%, and 24.66%, respectively. For PLA/BF specimens with a density of 0.9 g/cm³, the addition of continuous fibers led to increases of 36.36%, 46.43%, and 49.54% in compressive strength, modulus, and strain energy density, respectively. Similarly, in PLA/BF specimens with a density of 0.5 g/cm³, these property parameters increased by 44.44%, 57.02%, and 24.19%, respectively. Therefore, the addition of continuous fibers significantly enhanced the strength and modulus, effectively compensating for the decrease in material properties caused by foaming. To further characterize energy absorption, force-displacement curves were analyzed to derive mean crushing force (MCF) and specific energy absorption (SEA). The results (provided in Appendix A) show that continuous fiber reinforcement improved MCF by 50% and SEA by 24%–49% compared to pure foamed PLA, consistent with the stress-strain trends in Fig. 11.

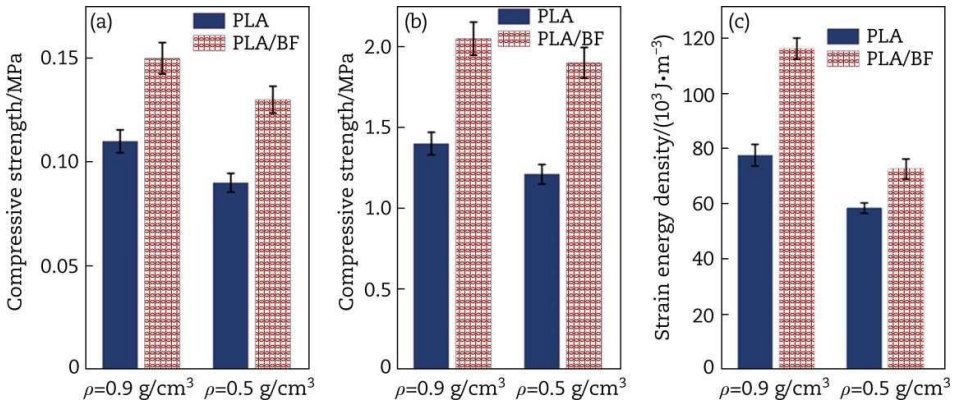

Fig. 11. Compressive strength (a), modulus (b), and strain energy density (c) of PLA and PLA/BF specimens at two densities

4. Conclusions

This study comprehensively explored the effects of incorporating fibers and adjusting printing parameters on key characteristics of these foamed composites, including printing accuracy, density, expansion ratio, and interlayer behavior. Moreover, the study demonstrated the compensatory effect of continuous fibers on reducing the strength of foamed PLA. The main conclusions are as follows:

(1) Fiber-reinforced foamed composites maintained the expansion ratio variation trend of PLA and provided good interlayer bonding and fiber impregnation through foaming. It allowed for printing parameters to be adjusted to achieve various expansion ratios and densities. Increasing the temperature from 190 °C to

270 °C resulted in a 53.27% decrease in maximum density due to changes in the interlayer gap, foam content, and diameter influenced by the printing temperature and layer height.

(2) An accurate prediction method for printing parameters was proposed based on the relationship between the print accuracy and foaming behavior. This method effectively calculated the necessary printing temperature and layer height to attain a desired design density and an excellent print accuracy, resulting in a density error of only −4.00% in the printed specimens. The application of this approach during production effectively minimized the possible decreases in mechanical characteristics caused by interlayer gaps.

(3) The reinforcement provided by continuous fibers compensated for the reduction in mechanical properties caused by the increased expansion ratio of the PLA material. The compression test results showed a significant enhancement in material properties with the addition of continuous fibers. Specifically, the foamed composite performed remarkable increases in the compressive strength, modulus, and strain energy density by 44.44%, 57.02%, and 26.52%, respectively, compared to foamed PLA. These exceptional properties underscore the potential for rail transportation, where lightweight, high-performance solutions are critical for enhancing energy efficiency and structural integrity.

Author Contributions

Kui Wang: Conceptualization, Methodology, Writing − Review and editing, Supervision; **Xinru Li:** Conceptualization, Methodology, Data curation, Writing − Original draft; **Ping Ching:** Methodology, Writing − Review and editing, Supervision; **Donghua Zhao:** Methodology, Writing − Review and editing; **Yi Xiong:** Validation; **Wei Wen:** Supervision; **Yong Peng:** Validation; **Said Ahzi:** Validation.

Acknowledgements

The authors would like to acknowledge the financial support of the Natural Science Foundation of Hunan (2024JJ5434) and the Postdoctoral Fellowship Program of CPSF (No. GZC20240646).

Appendix.

A：The expanding mechanical evaluation metrics of mechanical properties (SEE Fig. A1).

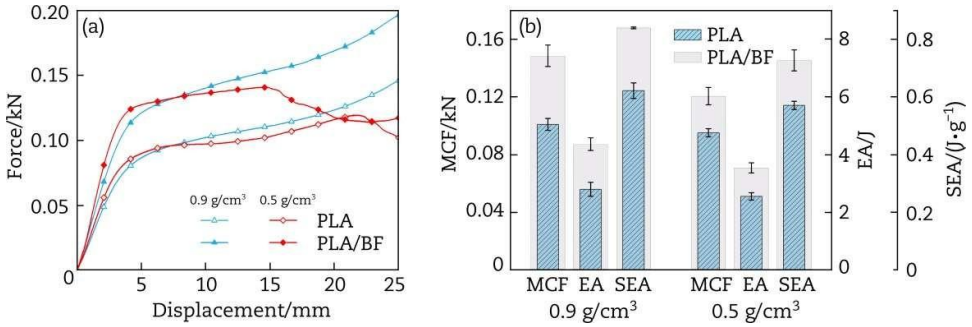

Fig. A1. Force-Displacement curves (a) and MCF, EA and SEA of PLA and PLA/BF specimens at two densities (b)

References

1. Coste G, Negrell C, Caillol S. From gas release to foam synthesis, the second breath of blowing agents. *Eur Polym J* 2020;**140**:110029.
2. Mohebbi A, Mighri F, Ajji A, et al. Current issues and challenges in polypropylene foaming: a review. *Cell Polym* 2015;**34**:299–338.
3. Ramsteiner F, Fell N, Forster S. Testing the deformation behaviour of polymer foams. *Polym Test* 2001;**20**:661–70.
4. Yousefi Kanani A, Kennedy A. Effect of the material extrusion process parameters on the compressive properties of additively manufactured foamed and nonfoamed polylactic acid structures. *3D Print Addit Manuf* 2024;**11**:207–18.
5. Jin FL, Zhao M, Park M, et al. Recent trends of foaming in polymer processing: a review. *Polymers* 2019;**11**:953.
6. Ren Q, Wu M, Weng Z, et al. Lightweight and strong gelling agent-reinforced injection-molded polypropylene composite foams fabricated using low-pressure CO_2 as the foaming agent. *J CO2 Util* 2021;**48**:101530.
7. Wang J, Chen D. Flexural properties and morphology of microcellular-insert injection molded all-polypropylene composite foams.

Compos Struct 2018;**187**:403–10.
8. Henton D, Gruber P, Lunt J, et al. Polylactic Acid Technology. *Advanced Materials* 2000;12:1841–6.
9. Ameli A, Nofar M, Jahani D, et al. Development of high void fraction polylactide composite foams using injection molding: crystallization and foaming behaviors. *Chem Eng J* 2015;**262**:78–87.
10. Elsawy MA, Kim KH, Park JW, et al. Hydrolytic degradation of polylactic acid (PLA) and its composites. *Renew Sustain Energy Rev* 2017;**79**:1346–52.
11. Rokkonen T, Willberg-Keyriläinen P, Ropponen J, et al. Foamability of cellulose palmitate using various physical blowing agents in the extrusion process. *Polymers* 2021;**13**:2416.
12. Rojas A, Torres A, López de Dicastillo C, et al. Foaming with $scCO_2$ and impregnation with cinnamaldehyde of PLA nanocomposites for food packaging. *Processes* 2022;**10**:376.
13. Gao X, Chen Y, Chen P, et al. Supercritical CO_2 foaming and shrinkage resistance of thermoplastic polyurethane/modified magnesium borate whisker composite. *J CO2 Util* 2022;**57**:101887.
14. Nofar M, Utz J, Geis N, et al. Foam 3D printing of thermoplastics: a symbiosis of additive manufacturing and foaming technology. *Adv Sci* 2022;**9**:2105701.
15. Kalia K, Francoeur B, Amirkhizi A, et al. *In situ* foam 3D printing of microcellular structures using material extrusion additive manufacturing. *ACS Appl Mater Interfaces* 2022;**14**:22454–65.
16. Tammaro D, Villone MM, Maffettone PL. Microfoamed strands by 3D foam printing. *Polymers* 2022;**14**:3214.
17. Bedarf P, Dutto A, Zanini M, et al. Foam 3D printing for construction: a review of applications, materials, and processes. *Autom Constr* 2021;**130**:103861.
18. Pawar A, Ausias G, Corre YM, et al. Mastering the density of 3D printed thermoplastic elastomer foam structures with controlled temperature. *Addit Manuf* 2022;**58**:103066.
19. Liu W, Wu X, Chen X, et al. Flexibly controlling the polycrystallinity and improving the foaming behavior of polylactic acid *via* three strategies. *ACS Omega* 2022;**7**:6248–60.
20. Wang G, Zhao J, Wang G, et al. Strong and super thermally insulating *in situ* nanofibrillar PLA/PET composite foam fabricated by high-pressure microcellular injection molding. *Chem Eng J* 2020;**390**:124520.
21. Xiang P, Gou L, Zou Y, et al. A facile strategy for preparation of strong tough poly(lactic acid) foam with a unique microfibrillated bimodal micro/nano cellular structure. *Int J Biol Macromol* 2022;**199**:264–74.
22. Vorawongsagul S, Pratumpong P, Pechyen C. Preparation and foaming behavior of poly (lactic acid)/poly (butylene succinate)/cellulose fiber composite for hot cups packaging application. *Food Packag Shelf Life* 2021;**27**:100608.
23. Wang J, Chai J, Wang G, et al. Strong and thermally insulating polylactic acid/glass fiber composite foam fabricated by supercritical carbon dioxide foaming. *Int J Biol Macromol* 2019;**138**:144–55.
24. Cheng P, Wang K, Peng Y, et al. Effects of cellular crossing paths on mechanical properties of 3D printed continuous fiber reinforced biocomposite honeycomb structures. *Compos Part A Appl Sci Manuf* 2024;**178**:107972.
25. Cheng P, Peng Y, Li S, et al. 3D printed continuous fiber reinforced composite lightweight structures: a review and outlook. *Compos Part B Eng* 2023;**250**:110450.
26. Damanpack AR, Sousa A, Bodaghi M. Porous PLAs with controllable density by FDM 3D printing and chemical foaming agent. *Micromachines* 2021;**12**:866.
27. Farzadi A, Solati-Hashjin M, Asadi-Eydivand M, et al. Effect of layer thickness and printing orientation on mechanical properties and dimensional accuracy of 3D printed porous samples for bone tissue engineering. *PLoS One* 2014;**9**:e108252.
28. Riou M, Ausias G, Grohens Y, et al. Thermoplastic foaming with thermo-expandable microcapsules: mathematical modeling and numerical simulation for extrusion process. *Chem Eng Sci* 2020;**227**:115852.
29. Rostami-Tapeh-Esmaeil E, Shojaei S, Rodrigue D. Mechanical and thermal properties of functionally graded polyolefin elastomer foams. *Polymers* 2022;**14**:4124.
30. Zhai W, Hu B, Li M, et al. Dimensional accuracy control and compressive property of microcellular polyetherimide honeycomb foams manufactured by an *in situ* foaming fused deposition modeling technology. *Adv Eng Mater* 2021;**23**:2001449.
31. Zha Y, Ma Q, Gan X, et al. Deformation and energy absorption characters of Al-CFRP hybrid tubes under quasi-static radial compression. *Polym Compos* 2020;**41**:4602–18.
32. Xu P, Lan X, Zeng C, et al. Compression behavior of 4D printed metamaterials with various Poisson's ratios. *Int J Mech Sci* 2024;**264**:108819.
33. Cheng P, Wang K, Chen X, et al. Interfacial and mechanical properties of continuous ramie fiber reinforced biocomposites fabricated by *in situ* impregnated 3D printing. *Ind Crops Prod* 2021;**170**:113760.
34. Yao TT, Liu YT, Zhu H, et al. Controlling of resin impregnation and interfacial adhesion in carbon fiber/polycarbonate composites by a spray-coating of polymer on carbon fibers. *Compos Sci Technol* 2019;**182**:107763.